文章编号: 1001 - 9014(2017)04 - 0408 - 07

DOI:10.11972/j.issn.1001 - 9014.2017.04.006

Three-dimensional near-field surveillance imaging using W-band system

CHENG Hang, ZHENG Hai-Tao, JING Han-Dan, LI Shi-Yong, SUN Hou-Jun*

(School of Information and Electronics, Beijing Institute of Technology, Beijing 100081, China)

Abstract: A W-band stepped-frequency three-dimensional near-field surveillance imaging system together with an effective radar imaging algorithm is presented. W-band signal is able to penetrate common clothing barriers to form an image of a person as well as any concealed items. Performing the image reconstruction procedure in the frequency - wavenumber domain, the algorithm is able to completely compensate the wavefront curvature in the near field through interpolation process. The interpolation relationship in frequency - wavenumber domain between sampled data and desired data was demonstrated. Moreover, the difference between algorithm model and experimental data are revealed. High range resolution and lateral resolution were obtained by emitting wideband stepped frequency signal and adopting high operating frequency. The cross-range resolution of the imaging result is better than 5 mm. The scheme of imaging system is described in detail along with a set of imaging results to show its superior imaging precision and sensitivity compared with existing Ka-band equipment.

Key words: millimeter-wave (MMW) imaging, near-field imaging, personnel surveillance, three-dimensional imaging, W-band system

PACS: 84.40.-x

W波段三维近场安检成像系统

程 航, 郑海涛, 敬汉丹, 李世勇, 孙厚军*

(北京理工大学 信息与电子学院,北京 100081)

摘要:介绍了一套基于频率步进机制的W波段三维近场安检成像系统以及相应的成像算法.W波段信号可以穿透普通衣物,对人员携带的藏匿物品进行成像.成像算法通过在频率波数域进行插值处理可以完全补偿近场的波前曲面.文中阐述了频率波数域的插值过程以及实验数据的预处理过程.成像系统通过发射宽带信号得到高分辨距离像,通过提高工作频率得到高分辨方位像,方位向分辨率优于5 mm.成像实验结果表明该系统性能优于现有的Ka波段成像系统.

关 键 词:毫米波成像;近场成像;人体安检;三维成像;W波段系统

中图分类号:TN957.52 **文献标识码**:A

Introduction

Millimeter-wave imaging has been actively investigated due to its unique features such as non-ionizing, transparent to clothing and potential for high resolution. Therefore, various applications of millimeter-wave imaging have been widely adopted in the world's counterterrorism actions while they also reconcile privacy[1-7]. In comparison with this emerging approach, conventional methods for individual surveillance, including manual detection, metal detectors and X-ray systems, have also been proved effective, only that a number of shortcomings cannot be neglected. For example, manual detection is inefficient and involves privacy issues; metal detectors cannot detect nonmetal threats such as plastic or liquid explosives, while it also causes nuisance alarms because of its incapability to distinguish innocuous metal items such as belt buckles, keys, etc.; X-ray system is widely used in luggage scanning, but it cannot be applied to personnel surveillance since its ionizing radiation may cause health problems[8]. As a result, millimeter-waves

Received date: 2016-12-02, **revised date**: 2017-04-07 **收稿日期**:2016-12-02, **修回日期**:2017-04-07

Biography: CHENG Hang (1987-), male, Xinjiang China. Ph. D. Research interests include millimeter-wave radar, radar imaging and SAR signal processing. E-mail: chenghang1031@126.com

* **Corresponding author**: E-mail: sunhoujun@bit.edu.cn

are relatively superior as it can readily penetrate common clothing material and be reflected from the human body as well as any concealed items to form an image of both; non-ionizing traits make it pose no known health hazard at moderate power levels. Additionally, the relatively shorter wavelength of millimeter-wave imaging system enables a high resolution potential in practice. Therefore, it is a proper technique to realize personnel security inspection using millimeter-wave imaging system[9-11].

The current millimeter-wave imaging systems consist of two fundamentally different types, passive and active. The passive imaging systems use receivers to acquire the radiation energy of the target and then utilize the brightness temperature to discriminate the target against the background. It is capable of achieving real-time 2-D imaging[12-16]. However, the resolution of passive imaging system is constrained by the antenna beamwidth, so the resolution is usually too low to recognize the shape of the target, not to mention that the indoor environment would dramatically decline the performance of passive imaging system[17]. Active imaging techniques use transceivers to illuminate the target and scan over a 2-D aperture. As the wideband signal is transmitted, the reflected complex signal is received at each discretely sampled position on the 2-D aperture, which means both amplitude and phase of the returned signal are recorded. The recorded data can be used to mathematically reconstruct a focused 3-D image of the target's reflectivity function. Employing the near-field synthetic aperture radar theory, the active imaging technique can provide higher resolution and better imaging quality than the passive imaging system does.

The higher resolution active imaging system has been developed broadly in recent years. For instance, the Pacific Northwest National Laboratory has invented both planar and cylindrical KA-band wideband imaging systems[9-11]. Given that the lateral resolution is influenced by the wavelength, antenna beamwidths, size of aperture and distance from aperture to target, the lateral resolution can be improved by increasing the operating frequency. The current existing active imaging systems mainly operate on Ka-band due to the fabrication techniques and cost, and terahertz technology has difficulties with stable sources and detectors with acceptable cost. As a result, W-band is a preferable choice to achieve higher resolution.

To improve the lateral resolution of the three-dimensional near-field surveillance imaging system, a W-band wideband active 3-D imaging system is presented. The algorithm of image reconstruction is demonstrated in detail with sampling and resolution analysis. Some related experiment results are given to validate the efficacy of the algorithm and the imaging system. The lateral resolution can be better than 5 mm. We also reveal the difference between algorithm model and experimental data, which is crucial to achieve a fully focused imaging result.

1 Wide-band image reconstruction

The wideband image reconstruction algorithm for personnel surveillance is similar to synthetic aperture radar (SAR) algorithm[18-20], except that the SAR algorithms are generally based on far-field assumption. For personnel surveillance, no far-field approximation is made due to large-aperture close-range operation. The wideband image reconstruction algorithm has been discussed and derived in[9], which is based on decomposing the spherical wave into a superposition of plane-wave components. The derivation presented in this section utilizes Principle of Stationary Phase (POSP), which is much clear from the perspective of signal processing.

1.1 Wide-band image reconstruction algorithm

The measurement configuration is shown in Fig. 1: the transceiver is assumed to be at position (x',y',Z_1), and a general point on the target is assumed to be at position (x,y,z), the target is assumed to be characterized by a reflectivity function $f(x,y,z)$, which is simply the ratio of reflected field to incident field.

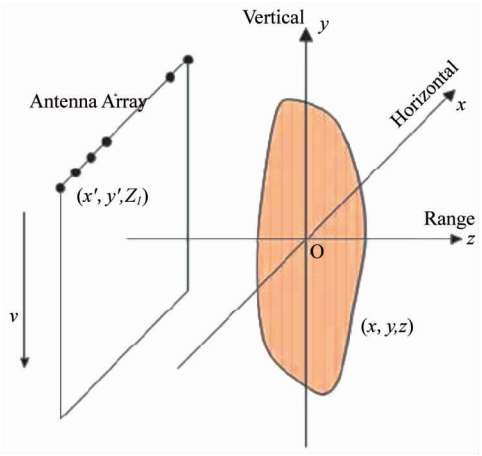

Fig. 1 Wide-band imaging system configuration
图 1 宽带成像系统示意图

The base band signal at the transceiver will simply be the superposition of each point on the target multiplied by the roundtrip phase to that point.

$$s(x',y',k) = \iiint f(x,y,z)\,\mathrm{e}^{-\mathrm{j}2k\sqrt{(x-x')^2+(y-y')^2+(z-Z_1)^2}}\,\mathrm{d}x\mathrm{d}y\mathrm{d}z \quad (1)$$

The wavenumber is denoted by $k=\omega/c$, where ω is the angular frequency and c is the speed of the light.

Transform Eq. 1 with 2-D spatial Fourier transformation

$$S(k_{x'},k_{y'},k) = \iiint f(x,y,z)\,\mathrm{d}x\mathrm{d}y\mathrm{d}z \times \iint \exp(-\mathrm{j}2kR)\exp[-\mathrm{j}(k_{x'}x'+K_{y'}y')]\,\mathrm{d}x'\mathrm{d}y' \quad (2)$$

where $R=\sqrt{(x-x')^2+(y-y')^2+(z-Z_1)^2}$.

Use principle of stationary phase (POSP) to calculate Eq. 2. The amplitude is not considered in this case since it will have little impact on focusing the image[9]. Drop the distinction between the primed and unprimed coordinate system:

$$\iint \exp(-\mathrm{j}2kR)\exp[-\mathrm{j}(k_{x'}x'+K_{y'}y')]\,\mathrm{d}x'\mathrm{d}y' = \exp[-\mathrm{j}\sqrt{4k^2-k_x^2-k_y^2}(z-Z_1)-\mathrm{j}k_xx-\mathrm{j}k_yy] \quad (3)$$

Rewrite Eq. 2 with Eq. 3:

$$S(k_x,k_y,k) = \mathrm{e}^{\mathrm{i}\sqrt{4k^2-k_x^2-k_y^2}Z_1}\iiint_{\times \mathrm{e}^{-\mathrm{j}k_x x}\mathrm{e}^{-\mathrm{j}k_y y}\mathrm{e}^{-\mathrm{j}\sqrt{4k^2-k_x^2-k_y^2}z}}^{f(x,y,z)} \mathrm{d}x\mathrm{d}y\mathrm{d}z \quad . \quad (4)$$

Define $k_z = \sqrt{4k^2 - k_x^2 - k_y^2}$,

$$S(k_x,k_y,k) = \mathrm{e}^{\mathrm{i}k_z Z_1}\iiint_{\times \mathrm{e}^{-\mathrm{j}k_x x}\mathrm{e}^{-\mathrm{j}k_y y}\mathrm{e}^{-\mathrm{j}k_z z}}^{f(x,y,z)} \mathrm{d}x\mathrm{d}y\mathrm{d}z \quad . \quad (5)$$

Transform Eq. 5 with 3-D spatial inverse Fourier transformation:

$$\begin{aligned} f(x,y,z) &= \iiint_{\times \mathrm{e}^{-\mathrm{j}k_z Z_1}\mathrm{e}^{-\mathrm{j}k_x x}\mathrm{e}^{-\mathrm{j}k_y y}\mathrm{e}^{-\mathrm{j}k_z z}}^{S(k_x,k_y,k)} \mathrm{d}k_x\mathrm{d}k_y\mathrm{d}k_z \\ &= \mathrm{IFFT}_{3D}\left[S(k_x,k_y,k)\mathrm{e}^{-\mathrm{j}k_z Z_1}\right] \\ &= \mathrm{IFFT}_{3D}\left[\mathrm{IFFT}_{2D}\left[s(x',y',k)\right]\mathrm{e}^{-\mathrm{j}k_z Z_1}\right]z \quad . \quad (6) \end{aligned}$$

The exponential term $\mathrm{e}^{-\mathrm{j}k_z Z_1}$ can be regarded as a matched filter. Therefore, we obtain the 3-D focused image of target's reflectivity function.

1.2 Interpolation

Equation 6 is valid to reconstruct the image if the data are defined continuously in x', y' and k. However, for practical imaging configurations, the data will be discretely sampled at uniform intervals of position and frequency. Therefore, the data $S(x',y',k)$ are assumed to be uniformly sampled in each variable. After 2D Fast Fourier Transform (FFT), a uniformly sampled version of $S(k_x,k_y,k)$ is obtained. Because the wavenumber k is a function of k_x, k_y and k_z, the data $S(k_x,k_y,k)$ contains samples of $S(k_x,k_y,k_z)$. However, the samples are not uniformly spaced in k_z. The samples is uniformly spaced in k_x and k_y, and will lie on concentric spheres of radius $2k$.

The interpolation relationship in wavenumber domain is shown in Fig. 2. The horizontal axis represents k_x and k_y, the vertical axis represents k_z. The concentric arcs represent $2k$ corresponding to the bandwidth of transmitted signal. The vertical dashed lines represent uniformly sampling position in k_x and k_y, and the horizontal dashed lines mean uniformly sampling position in k_z.

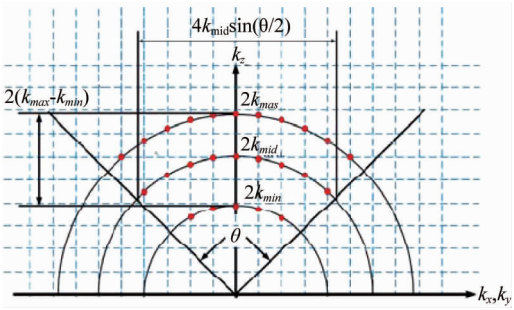

Fig. 2 Interpolation relationship in wavenumber domain

图2 波数域插值关系

The nodes of vertical dashed lines and arc, which are marked by red dots, represent the sample position in wavenumber domain that we obtained from the received signal. The nodes of vertical dashed lines and horizontal dashed lines represent interpolation position, at which we need to sample in order to operate the inverse 3-D FFT in Eq. 6. The data need to be resampled at uniformly spaced positions in k_z. This is easily accomplished using interpolation techniques.

Based on discrete sampled data, interpolation techniques can reconstruct a continuous signal. A lot of interpolation models can be selected to deal with the computation such as sinc interpolation, liner interpolation and spline interpolation. Different models will affect accuracy and processing time.

1.3 Sampling criterion and image resolution

The discretization of the signal must satisfy the Nyquist sampling criterion. As illustrated in Fig. 2, the bandwidth of synthetic aperture is approximately $4k_{\mathrm{mid}}\sin(\theta/2)$, which is determined by a number of factors including the wavelength, size of the aperture, size of he target, and distance to the target. The θ is the lesser of the full beamwidth of the antenna or the angle subtended by the aperture. The worst case will occur when a target locates very near to the aperture and the sample point is near the edge of aperture, which will lead the θ to approach 180°. In the worst scenario, the sampling criterion can be expressed as:

$$\Delta x \approx \frac{2\pi}{4k_{\mathrm{mid}}\sin(\theta/2)} < \frac{\lambda_{\min}}{4} \quad , \quad (7)$$

where $\lambda_{\min}$ is the shortest wavelength of the transmitted signal.

The criterion Eq. 7 is more restrictive than usually required. Because in the practical imaging system, the θ is seldom to approach 180° due to either the moderate distance from target to aperture or the limited antenna beamwidth. For this reason, the sampling criterion can often employ sampling intervals in the order of $\lambda_{\min}$.

The required frequency sampling is determined by the maximum unambiguous range:

$$\Delta f < \frac{c}{2R_{\max}} \quad , \quad (8)$$

where $R_{\max}$ is the maximum target range, Δf is the required frequency sampling interval.

The resolution obtained in the image can be determined by examining the extent or width of the spectrum coverage in the wavenumber domain. Generally, the wavenumber domain forms a sector region as shown in Fig. 2, so the uniform frequency coverage region is approximately regarded as rectangular with width of $4k_{\mathrm{mid}}\sin(\theta/2)$, which results in a spatial pulse width of $\delta x = 2\pi/4k_{\mathrm{mid}}\sin(\theta/2)$. Therefore, the cross-range resolution is:

$$\delta x = \delta y = \frac{\lambda_{\min}}{4\sin\left(\frac{\theta}{2}\right)} \quad , \quad (9)$$

where λ_{mid} is the wavelength at the center frequency.

The spatial frequency width in the k_z range is $2(k_{\max} - k_{\min})$, this approximately results in a resolution as

$$\delta z = \frac{2\pi}{2(k_{\max} - k_{\min})} = \frac{c}{2B} \quad , \quad (10)$$

where B is the bandwidth of the transmitted signal.

2 Imaging system composition

An imaging prototype, utilizing a 92 ~ 94 GHz wideband transceiver and a programmable planar scanner,

has been used to gather data to validate the performance of the algorithm and W-band system.

A block diagram of the imaging system is shown in Fig. 3. The transmitted signal is launched using a small wide-beamwidth conical horn antenna. The antenna and the transceiver are mounted on a fast large programmable mechanical scanner. The scan velocity is settable. While scanning, the scanner is emitting 3000 pulses in one second. By counting the pulses, the computer, which is connected with the scanner, calculates the position, and controls the transceiver to launch and receive the wideband signal through antenna at the sampling position, as well as controls the A/D converter to digitize the signal and store in the hard disk. In order to sample on a 2-D aperture, the computer will control the scanner to move to a new initial scan position, and start another linear scan. The 2-D aperture data is then formed as the input of the image reconstruction algorithm $s(x',y',k)$. The data processing module, typically a fast speed digital signal processor, will process the data. Finally, the image will display on the terminal UI.

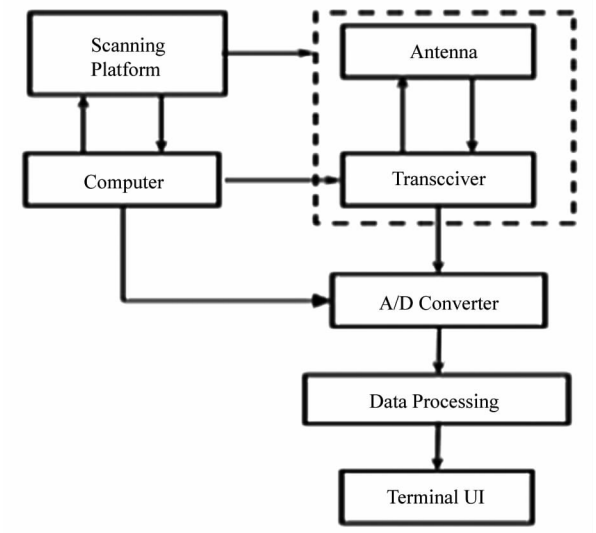

Fig. 3　Block diagram of the imaging system
图 3　成像系统结构框图

A photograph of the scanning system and a photograph of the antennas and transceiver are shown in Fig. 4. The system is quasi-monostatic, which means that the transmitting and receiving antenna are separate, but in approximately the same location and may be assumed to be coincident at the midpoint between the two antennas. The receiving antenna usually has the same size and type as the transmitting antenna and is placed immediately adjacent to the transmitting antenna. In this way, the pair of antennas simulates a single antenna, but with significantly higher transmit-receive isolation.

A simplified schematic of the transceiver is shown in Fig. 5. The system works with stepped frequency and operates in the W-frequency band. The exact operating configuration ranges from 92 to 94 GHz.

A 140 MHz single frequency signal is generated as the intermediate frequency (IF) using the Direct Digital Synthesizer (DDS) to ensure the coherent characteristic.

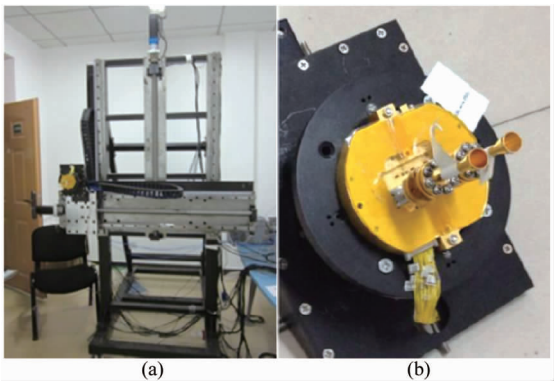

Fig. 4　(a) Photograph of the scanning system, (b) photograph of the antennas and transceiver
图 4　(a)扫描系统照片,(b)天线与收发机照片

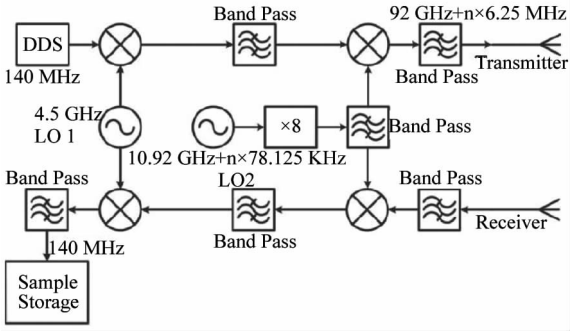

Fig. 5　Simplified schematic of the transceiver
图 5　收发机原理图

The first local oscillator operates at 4.5 GHz. The second local oscillator is as stepped frequency source and operates at 10.92 GHz. It rises 78.125 kHz in every Pulse Repetition Time (PRT). After passing the octupler and mixer, the signal transmits through the antenna. Regarding receiving channel, after down-converting with two oscillators, a 140 MHz intermediate signal is received.

The beamwidth of both transmitting antenna and receiving antenna are 38°. The aperture of the imaging system is 66 cm × 66 cm, and the distance to the target is approximately 1 m. The data are discretely sampled with typical dimensions of 220 x' samples, 220 y' samples, and 320 frequency samples with spatial and frequency step sizes of 3 mm (Δx), 3 mm (Δy), and 6.25 MHz (Δf), respectively. The frequency step size is less than Eq. (8) demanded in order to improve the Signal Noise Ratio (SNR) of the ultimate imaging results.

3　Experimental data processing

The experimental data are sampled at the intermediate frequency 140 MHz. In order to match the form in the Eq. 1, the sampled intermediate signal needs to be transformed to complex base band signal, which can be accomplished using digital down-convert techniques.

In Sect. 1, the phase variation in Eq. (1) is only related with spatial distance from target to antenna. How-

ever, in a practical imaging system, an additional phase variation will occur due to system delay. The signal we captured was not sampled immediately after received by the antenna. It was sampled by A/D converter after it went through the receive channel. A schematic diagram of system delay is shown in Fig. 6.

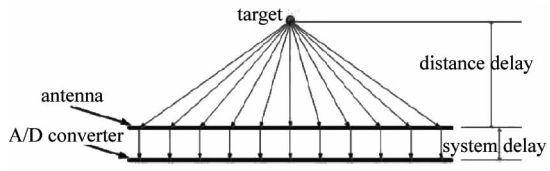

Fig. 6 Schematic diagram of system delay
图6 系统延时示意图

In terms of single frequency imaging system, the system delay will cause a constant phase variation, which could be ignored in subsequent processing. However, for wide band imaging system, the system delay will cause a linear phase variation in frequency domain that needs to be eliminated from the raw data before being put into algorithm. The system delay can be observed from high resolution range profile as shown in Fig. 7.

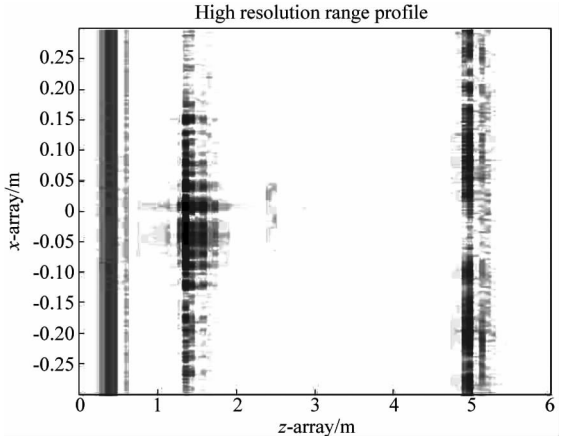

Fig. 7 High resolution range profile of raw data
图7 原始数据高分辨距离像

In Fig. 7, x-array represents a row of horizontal sampling positions and z-array represents range dimension. The power peak appearing near 0.4 m in z-array represents the coupled signal that should appear theoretically at 0m in z-array. The power peak appearing near 1.4 m in z-array represents the target that should appear near 1m in z-array. The power peak appearing near 5 m represents the wall of the laboratory. According to the high resolution range profile, the system delay causes a 0.4 m range cell migration in range dimension, which means the system delay is 2.67 ns.

To compensate the system delay, a matrix with the same size as raw data is fabricated.

$$C(x',y',,k) = \exp(j2kR(x',y')_{\text{delay}}) . \quad (11)$$

The raw data is multiplied by Eq. (11), where $R(x',y')_{\text{delay}}$ is the distance variation caused by system delay (in this case, 0.4 m). The $R(x',y')_{\text{delay}}$ usually vary if the system uses different T/R channel at different sampling position (x',y'). However, in this prototype, as we utilize one T/R component to mechanically scan over the 2-D aperture, the system delay was assumed to be the same at different sampling positions.

4 Experiment results

Some targets, such as metal balls, knives, scissors, transportation cards, have been tested through experiment. In addition to visible items, we have also tested the prototype's performance of detecting concealed items. All targets were bonded on foamed plastic. Then we put the targets right at the center of the aperture. The depth to the targets was approximately 1 m. The imaging results are showed from Figs. 8-11. The impact of system delay is also included. Note that all the images are originally reconstructed in 3D formation and normalized with maximum amplitude of itself. Dynamic range is 30 dB. All images can demonstrate focusing quality, but it is only able to show the relative reflectivity of the target. The 3D image is then collapsed using a maximum value projection into a fully focused 2D image of the target for display on the computer[9].

Figure 8 shows the photo and W-band imaging results of ten metal balls embedded in the foamed plastic, the radius of which is 1 cm. For the raw data without system delay compensation, according to the discussion in Sec. 3, the focusing quality is severely poor. From the imaging result with system delay compensation, the target features, such as position and space between balls, can be clearly identified. The imaging result can comprehensively represent characteristics of the target. The measured azimuth-range and elevation-range resolutions are $\Delta x = 0.36$ cm, $\Delta y = 0.48$ cm, respectively.

Figure 9 shows the photo and W-band imaging result of a scissor and a knife stably nailed in foamed plastic. The imaging result is quite similar to optical photo. Inspectors could easily recognize the shape of the target. Furthermore, the nails located at both handle of the scissor and the branch of the knife can be clearly seen due to high resolution, so does the metal chain at the tail of the knife.

Figure 10 shows the photo and W-band imaging result of the transportation card which is bonded on foamed plastic by tapes. The system can penetrate the plastic surface and detect the internal chip at the upright corner of the card. The tape can also be shown in the imaging result.

Figure 11 shows the photo and W-band imaging result of a concealed knife covered by a cotton T-shirt. This experiment simulates a practical situation to test the detecting performance of the imaging system. Fine details are apparent in the millimeter-wave imaging that we can clearly recognize the striation of the T-shirt, and concealed knife is also easy to identify in the image. The targets appearing at the bottom of the image is due to the periodic assumption of FFT. The imaging result sufficiently demonstrates the detecting capability of the wideband millimeter-wave imaging system.

5 Conclusions

This paper has presented an effective W-band 3-D

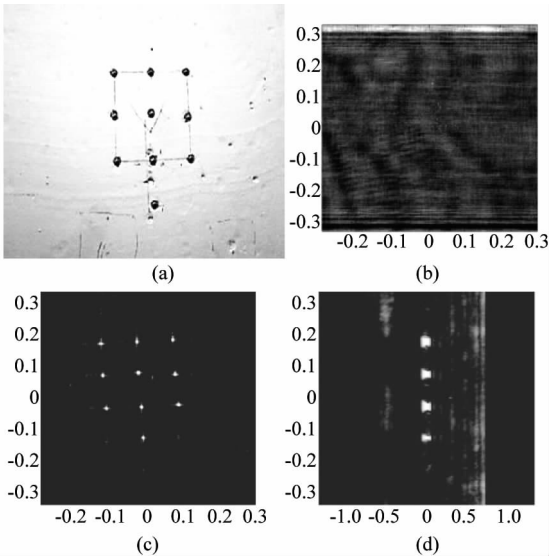

Fig. 8 (a) Photo of experimental target, (b) imaging result (azimuth-elevation projected) without system delay compensation, (c) imaging result (azimuth-elevation projected) with system delay compensation, (d) range-elevation projected imaging result with system delay compensation

图 8 (a)实验目标照片,(b)未经系统延时补偿的成像结果(沿方位—高度投影),(c)经系统延时补偿后的成像结果(沿方位—高度投影),(d)经系统延时补偿后的成像结果(沿距离—高度投影)

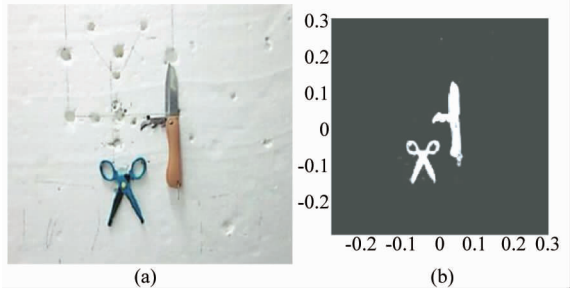

Fig. 9 (a) Photo of experimental target, (b) imaging result (azimuth-elevation projected) with system delay compensation

图 9 (a)实验目标照片,(b)经系统延时补偿后的成像结果(沿方位—高度投影)

imaging system for individual security surveillance. The system uses a coherent stepped frequency transceiver to scan over a large aperture, both horizontally and vertically; then the echo complex signal is used to reconstruct a 3-D focused image by 3-D image reconstruction algorithm. Further details have been described regarding the image reconstruction method and formulas used to form a focused image at near field, as well as the block diagram of the imaging system and schematic diagram of the transceiver. The emphasis about experimental data processing rather than simulation processing is the result of weighing priorities, because we are not able to obtain a fully focused image without compensating system delay. Finally,

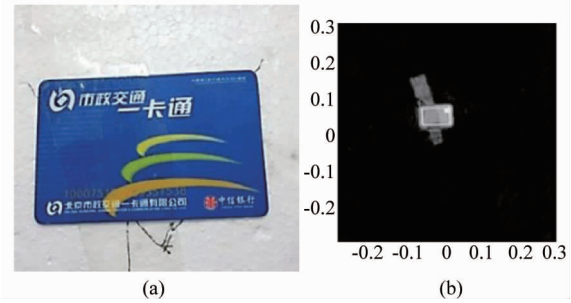

Fig. 10 (a) Photo of experimental target, (b) imaging result (azimuth-elevation projected) with system delay compensation

图 10 (a)实验目标照片,(b)经系统延时补偿后的成像结果(沿方位—高度投影)

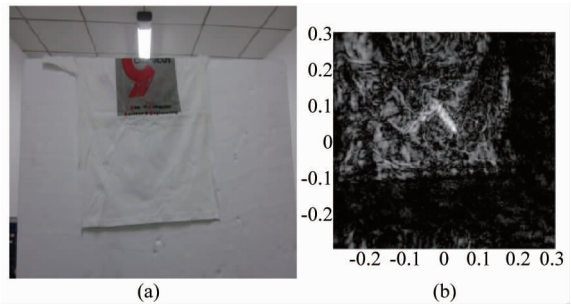

Fig. 11 (a) Photo of experimental target, (b) imaging result (azimuth-elevation projected) with system delay compensation

图 11 (a)实验目标照片,(b)经系统延时补偿后的成像结果(沿方位—高度投影)

a set of laboratory imaging results have been shown to demonstrate that high resolution, effectiveness and image fidelity are achievable by using millimeter-wave imaging technique. The cross-range resolution can be further improved by adopting a wide beamwidth antenna. With all that has been discussed and illustrated, we have concluded that the W-band 3-D imaging system can achieve higher resolution than major existing Ka-band active imaging systems, and is proven to be an efficient approach for personnel surveillance.

References

[1] Osumi N, Ueno K. Microwave holographic imaging method with improved resolution[J]. *Antennas and Propagation, IEEE Transactions on*, 1984, **32**(10):1018 - 1026.

[2] Zech C, Hülsmann A, Kallfass I, *et al*. Active millimeter-wave imaging system for material analysis and object detection[J]. *SPIE Security Defense. International Society for Optics and Photonics*, 2011: 81880D - 81880D - 9.

[3] Iizuka K, Gregoris L G. Application of microwave holography in the study of the field from a radiating source[J]. *Applied Physics Letters*, 1970, **17**(12): 509 - 512.

[4] Farhat N H, Guard W R. Millimeter wave holographic imaging of concealed weapons[J]. *Proceedings of the IEEE*, 1971, **59**(9):1383 - 1384.

[5] Corredoura P, Baharav Z, Taber B, *et al*. Millimeter-wave imaging

system for personnel screening: scanning 10^ 7 points a second and using no moving parts[C]//*Defense and Security Symposium. International Society for Optics and Photonics*, 2006: 62110B-62110B-8.
[6] Cooper K B, Dengler R J, Llombart N, *et al*. Penetrating 3-D imaging at 4-and 25-m range using a submillimeter-wave radar[J]. *Microwave Theory and Techniques, IEEE Transactions on*, 2008, **56**(12):2771-2778.
[7] Kemp M C. Millimetre wave and terahertz technology for the detection of concealed threats: a review[C]//*Optics/Photonics in Security and Defence. International Society for Optics and Photonics*, 2006: 64020D-64020D-19.
[8] Howells E R, Phillips D C, Rogers D. The probability distribution of X-ray intensities. II. Experimental investigation and the X-ray detection of centres of symmetry[J]. *Acta Crystallographica*, 1950, **3**(3): 210-214.
[9] Sheen D M, McMakin D L, Hall T E. Three-dimensional millimeter-wave imaging for concealed weapon detection[J]. *Microwave Theory and Techniques, IEEE Transactions on*, 2001, **49**(9):1581-1592.
[10] Collins H D, Gribble R P, Hall T E, *et al*. Real-time holographic surveillance system: U. S. Patent 5,455,590[P]. 1995-10-3.
[11] Sheen D M, Collins H D, Hall T E, *et al*. Real-time wideband holographic surveillance system," U. S. Patent 5 557 283, Sept. 17, 1996.
[12] Goldsmith P F, Hsieh C T, Huguenin G R, *et al*. Focal plane imaging systems for millimeter wavelengths[J]. *Microwave Theory and Techniques, IEEE Transactions on*, 1993, **41**(10):1664-1675.
[13] Luukanen A, Ala-Laurinaho J, Leivo M, *et al*. Developments towards real-time active and passive sub-millimeter wave imaging for security applications[C]//*Microwave Symposium Digest (MTT), 2012 IEEE MTT-S International. IEEE*, 2012:1-3.
[14] Abril J, Nova E, Broquetas A, *et al*. Combined passive and active millimeter-wave imaging system for concealed objects detection[C]/*Infrared Millimeter and Terahertz Waves (IRMMW-THz), 2010 35th International Conference on. IEEE*, 2010: 1-2.
[15] HAN Dong-Hao, LIU Hao, ZHANG De-Hai, *et al*. Passive submillimeter-wave imaging demonstrated by two-element interferometer[J]. *J. Infrared Millim. Waves*(韩东浩,刘浩,张德海,等. 干涉式被动亚毫米波成像系统. **红外与毫米波学报**), 2016, **35**(6):656-661.
[16] WANG Nan-Nan, QIU Jing-Hui, ZHANG Peng-Yu, *et al*. Passive millimeter wave focal plane array imaging technology[J]. *J. Infrared Millim. Waves*. (王楠楠,邱景辉,张鹏宇,等. 被动毫米波焦面阵成像技术研究. **红外与毫米波学报**), 2011, **30**(5):419-424.
[17] Coward P, Appleby R. Development of an illumination chamber for indoor millimeter-wave imaging[J]. *Proc SPIE*, 2003, **5077**:54-61.
[18] Edrich M, Weiss G. Second-generation Ka-band UAV SAR system [C]//*Microwave Conference*, 2008. *EuMC* 2008. 38*th European. IEEE*, 2008:1636-1639.
[19] Carrara W G, Goodman R S, Majewski R M. *Spotlight synthetic aperture radar signal processing algorithms*[M]. Boston: MA: Artech House, 1995.
[20] Bamler R. A comparison of range-Doppler and wavenumber domain SAR focusing algorithms[J]. *Geoscience and Remote Sensing, IEEE Transactions on*, 1992, **30**(4):706-713.

(上接第407页)

[9] Hughes M A, Suzuki T, Ohishi Y, *et al*. Compositional dependence of the optical properties of bismuth doped lead-aluminum-germanate glass [J]. Optical Materials, 2010, **32**(9):1028-1034.
[10] Peng M Y, Qiu J R, Chen D P, *et al*. Broadband infrared luminescence from Li_2O-Al_2O_3-ZnO-SiO_2 glasses doped with Bi_2O_3[J]. *Optics Express*, 2005, **13**(18):6892-6898.
[11] Chi G W, Zhou D C, Song Z G, *et al*. Effect of optical basicity on broadband infrared fluorescence in bismuth-doped alkali metal germanate glasses[J]. *Optical Materials*, 2009, **31**(6):945-948.
[12] Qiuchun Sheng, Xiaolin Wang, Danping Chen. Enhanced Luminescent Properties and Mechanism in a Novel Yb - Bi Co-doped Boro-phosphate Glass[J]. Materials Letters, 2012, **80**:135-137.
[13] Sheng Q C, Liu S, Li W T, *et al*. Enhanced broadband near-infrared luminescence and peak wavelength shift of Yb - Bi ions co-doped phosphate glasses containing Lu^{3+}[J]. *Journal of Luminescence*, 2013, **144**:26-29.
[14] Jiang Z W, Dai N L, Yang L Y, *et al*. Effects of Al_2O_3 composition on the near-infrared emission in Bi-doped and Yb-Bi-codoped silicate glasses for broadband optical amplification[J]. *Journal of Non-Crystalline Solids*, 2014, **383**:196-199.
[15] Dai N L, Xu B, Jiang Z W, *et al*. Effect of Yb^{3+} concentration on the broadband emission intensity and peak wavelength shift in Yb/Bi ions co-doped silica-based glasses[J]. *Optics Express*, 2010, **18**(18):18642-18648.
[16] Wang R F, Liu J, Zhang Z. Luminescence and energy transfer progress in Bi-Yb co-doped germanate glass[J]. *Journal of Alloys and Compounds*, 2016, **688**:332-336.
[17] Zhou D C, Wang R F, He X J, *et al*. Color-tunable luminescence of Eu^{3+} in PbF_2 embedded in oxyfluoroborate glass and its nanocrystalline glass[J]. *Journal of Alloys and Compounds*, 2015, **621**:62-65.
[18] Guan M J, Wang X, Zhuang Y X, *et al*. Abnormal luminescence behavior in Bi-doped borosilicate glasses[J]. *Journal of The Electrochemical Society*, 2011, **158**:151-154.
[19] Wang R F, Zhou D C, Zhao Z Y, *et al*. Effect of optical basicity on broadband infrared fluorescence in erbium-doped germanate glasses [J]. *Journal of Alloys and Compounds*, 2012, **513**:339-342.
[20] Wang R F, Yang Z W, Zhou D C, *et al*. Structure and luminescent property of Er^{3+}-doped germanate glasses[J]. *Journal of Non-Crystalline Solids*, 2014, **383**:200-204.